

Modelling and simulation in reactive polymer processing

This content has been downloaded from IOPscience. Please scroll down to see the full text.

2004 Modelling Simul. Mater. Sci. Eng. 12 S121

(<http://iopscience.iop.org/0965-0393/12/3/S06>)

View [the table of contents for this issue](#), or go to the [journal homepage](#) for more

Download details:

IP Address: 128.111.121.42

This content was downloaded on 09/07/2015 at 07:28

Please note that [terms and conditions apply](#).

TOPICAL REVIEW

Modelling and simulation in reactive polymer processing

José M Castro, Mauricio Cabrera Ríos¹ and Clark A Mount-Campbell

Department of Industrial, Welding, and Systems Engineering, The Ohio State University,
Columbus, Ohio 43210, USA

Received 29 September 2003

Published 19 April 2004

Online at stacks.iop.org/MSMSE/12/S121

DOI: 10.1088/0965-0393/12/3/S06

Abstract

Modelling and simulation in reactive polymer processing have been active research areas for the past decades in academic institutions as well as within the industry. Both areas have played a key role in advancing and optimizing reactive polymer processing operations. The objective of this paper is to review the two major classifications of models used to simulate polymer processes: physics based models and empirical models. Additionally, a section on multiple criteria optimization using data envelopment analysis has been included for completeness. The work presented here helps define a decision-making framework for the creation of reactive polymer process models and for the effective selection of settings of the process variables based on these models.

1. Introduction

Reactive polymer processing is an area where several physical and chemical phenomena interact. The need to understand, analyse, predict, and control the behaviour of these phenomena has been a fertile ground for academic and industrial research. Mathematical modelling and simulation have played a key role in advancing and optimizing reactive polymer processing operations. In general, one can distinguish two major types of mathematical models: those based on physical and/or chemical principles and those based on statistics, commonly called empirical models. A considerable amount of research has been devoted to modelling based on physical and chemical principles because of the insight that these models are capable of providing. However, when these models are not available or if their complexity precludes their widespread use, empirical models are needed.

A map of the decision sequence imbedded in general process modelling is presented in figure 1. The following discussion refers to this figure. In any modelling study, it is certainly the first step to determine what the phenomena that will be modelled are. The selection of

¹ Permanent address: Graduate Programme in Systems Engineering, Universidad Autónoma de Nuevo León, San Nicolás de los Garza, NL 66450, Mexico.

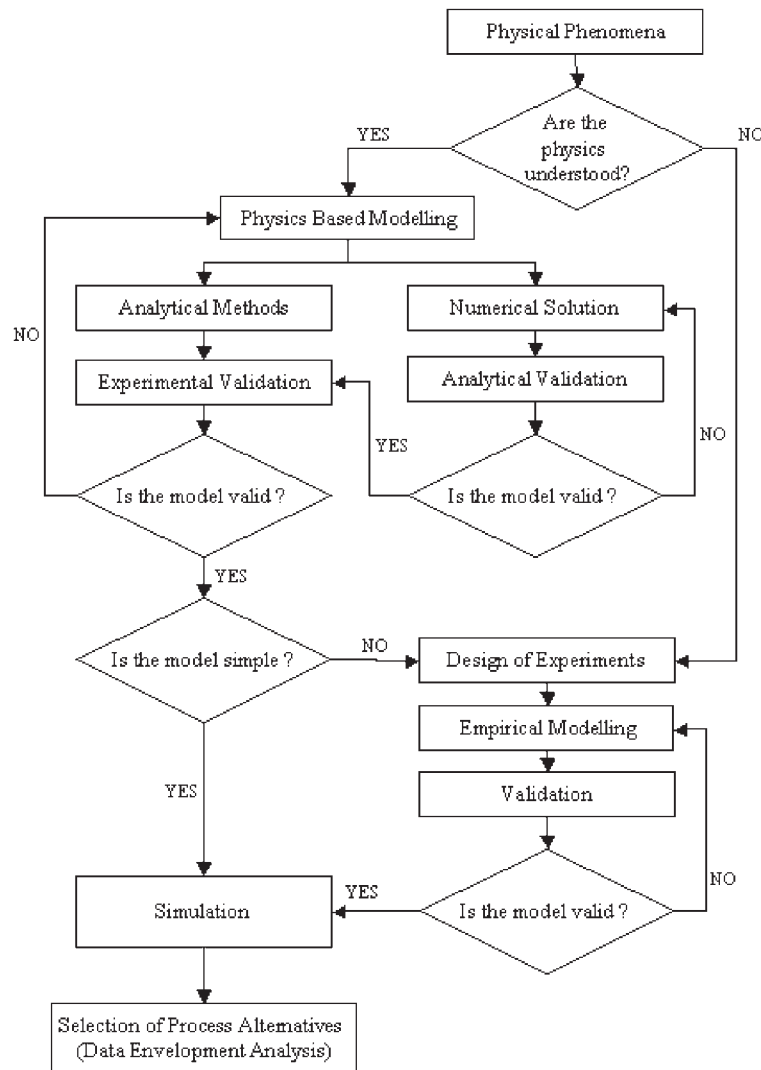


Figure 1. Decision-making flow diagram for process modelling.

these phenomena is usually determined by the analyst either based on conjectures about the importance of a particular behaviour observed in the process, or based on previous knowledge pointing towards important cause–effect relationships. Once the candidate phenomena have been identified, it is necessary to determine if the physics behind them are sufficiently understood and, perhaps, documented. The existence of scientific knowledge about the causality of our phenomena will lead to the path of physics modelling, while the lack of it, will lead to that of empirical modelling. The complexity of the physics based model will dictate if an analytical solution is feasible or if a numerical solution is required. In the case where a numerical solution is needed, before experimental validation, the numerical solution should be validated for extreme cases where analytical solutions can be obtained. The experimental validation is followed by an assessment of the burden to obtain predictions (i.e. to simulate) from a particular model. The result of this assessment will help determine whether it is convenient

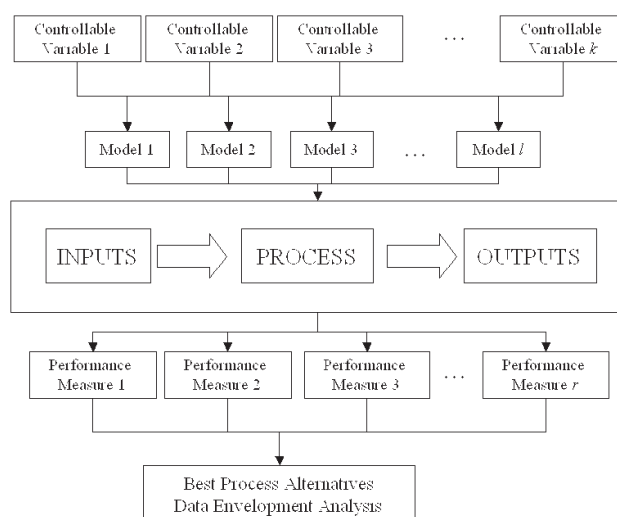


Figure 2. The definition of the best process alternatives.

to summarize the functionality of the physics based model with an empirical model, or if the physics based model is simple enough as to be used repeatedly to generate predictions. At the end, the model will be used to simulate a large number of combinations of untried variable levels to ultimately determine the best alternatives in terms of controllable variables for the process.

On the other hand, lack of scientific knowledge about the causality of a phenomenon of interest will entail the use of empirical models. Empirical modelling requires the use of statistical designs of experiments to experimentally establish the relationship between process variables and the physical phenomena. Notice that an appropriate validation is a required step in empirical modelling.

After following any of the branches, at the end one will have a model or a series of models that will be used to simulate the process to generate the required response predictions of the physical phenomena under study. Most likely, the end goal of the simulation is to find combinations of controllable variables in the process that allow producing parts with high performance value in specific measures. That is, the interest is on optimization.

In real production operations, there is commonly more than a single performance measure (PM) to optimize. In addition, many PMs exhibit conflicting behaviour when optimization is attempted, i.e. optimizing a PM only comes at detriment of another. The idea is, then, to find the best compromises between all PMs of interest. These best compromises become the process alternatives. That is precisely the goal of multiple criteria optimization. Data envelopment analysis (DEA) is one of the techniques that has been used to find these compromises [1–3]. A schematic representation on how to obtain the process alternatives is shown in figure 2. In this figure, the controllable variables affect the behaviour of different phenomena in the process. These relationships are mimicked by models, physics based and/or empirical, which are subsequently used to generate a number of predictions at different combinations of controllable variables' levels. These predictions are then used to find the best compromises through DAE, thus finding the best process alternatives.

Most manufacturing operations in reactive polymer processing involve at least two stages: shaping and solidification. In general, a liquid–solid phase change is involved. In contrast to

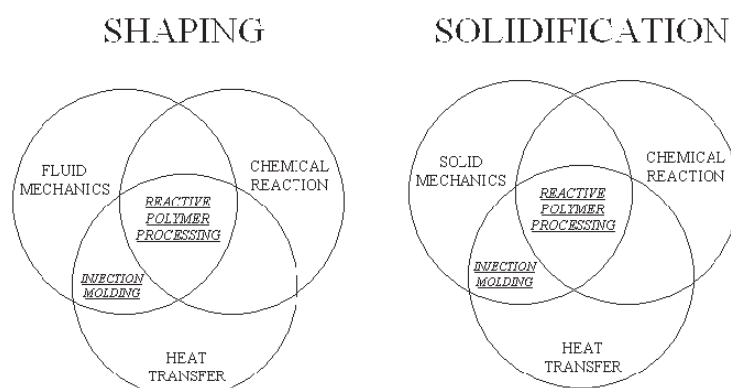


Figure 3. Phenomena involved at different stages of polymer processing.

thermoplastics moulding where solidification occurs through cooling of the material, in reactive polymer processing, solidification is due to chemical reaction. This difference can be visualized in figure 3. For example, injection moulding (IM) of thermoplastics starts by melting and mixing the raw material, after which the melt is forced into the mould cavity through an injection gate. The geometry of the mould cavity corresponds to the desired shape of the final part, therefore once the mould has been filled, the part is left to solidify by cooling before ejection. On the other hand, in compression moulding of sheet moulding compound (SMC), a preform usually conformed by a thermosetting resin and reinforcement, during shaping, the SMC is compressed inside a heated mould forcing the material to completely fill the cavity. As the reactive resin undergoes crosslinking, the part solidifies through this chemical reaction to be demoulded next. Compression moulding of SMC is considered to be a reactive polymer process.

Referring to figure 3, it is possible to identify the phenomena that are important on each processing stage of IM and reactive polymer processing. Figure 3 also helps to realize the high degree of coupling that exists between multiple phenomena. Coupled phenomena make modelling considerably more challenging; therefore their identification is critical on early stages. Determining the amount and the nature of coupling can lead to great reduction in the modelling effort.

One possible way to assess the degree of coupling between several phenomena is provided by scaling analysis. Scaling is a process that begins with the linear transformation of variables describing a physical phenomenon to take values in a range from 0 to 1. This process allows one to compare the different terms of a model under a pure magnitude framework, and thus, to discriminate between relatively dominant and negligible terms. Model simplification achieved through scaling can also lead to determine characteristic values of the process variables involved, and certainly to obtain well-known dimensionless groups. A concise treatment on scaling can be found in Dantzig and Tucker [4]. The relevant dimensionless groups in polymer processing are discussed in Castro and Lee [5].

The following sections explain, with the aid of case studies, the approach to different modelling situations. For completeness, the final section of this document explains the use of DEA to solve multiple criteria optimization problems in reactive polymer processing.

2. Physics models

There are many advantages to producing physics based models of phenomena of interest. Building a physics based model always helps increase the understanding and enhances the

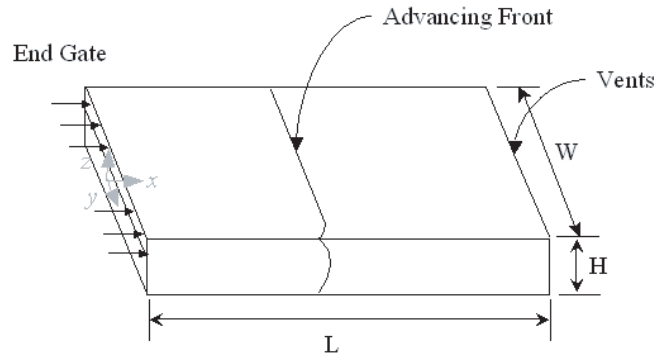


Figure 4. Rectangular mould with end gate ($W/H \gg 1$).

analysis capabilities. Even when a solution is not readily available from a physics model, the model-building process can provide important information about the degree and nature of coupling between different phenomena. The decision process in figure 1 shows the emphasis on creating physics models even if convenience leads to their replacement with empirical models.

Next, an example in reaction IM (RIM) for a simple geometry part is presented to discuss physics based models and the effective use of scaling analysis [6]. The rectangular mould with an end gate under consideration is shown in figure 4. RIM, as its name implies, consists of the injection of a reactive liquid into a mould cavity for shaping. In this case, the part solidifies by chemical reaction. In the traditional RIM process, the reactive species are mixed on line by impingement mixing just before entering the mould. We will limit our discussion to the filling (shaping) and solidification (curing) stages. The mixing aspects of RIM are reviewed in [7–9]. The moulding pressure will be determined by the filling stage, and the cycle time by the curing stage. It is easy to see that at the end it is desirable to reduce both the required moulding pressure and the cycle time.

The example presented here focuses on the required moulding pressure [6], an equivalent analysis for the cure time can be found in [10]. This case illustrates how by doing some *a priori* scaling analysis the modelling effort can be greatly simplified. For analysis purposes, the flow is divided into two subdomains: main flow, where the material particles have nearly straight path lines, and the flow front, which gives a fountain effect [11–13]. The assumptions of the model for the main flow, which will be the focus of this example are: (1) constant thermal properties, (2) negligible molecular diffusion, (3) second-order kinetics with Arrhenius temperature dependence, (4) Newtonian fluid, (5) constant density, (6) laminar flow, (7) negligible entrance effects, (8) constant flow rate, (9) negligible side wall effects, (10) unidirectional flow, and (11) negligible heat conduction in the x - and y -directions.

The balance of linear momentum in the x -direction in terms of dimensionless variables is

$$\frac{HRe}{2L} \left(\frac{\partial v_x^*}{\partial t^*} \right) = - \left(\frac{\partial p}{\partial x} \right)^* + \frac{\partial}{\partial z^*} \left(\eta^* \frac{\partial v_x^*}{\partial z^*} \right) \quad (1)$$

where H and L are the thickness and length of the mould, respectively; v_x^* is the dimensionless velocity in the x -direction, v_x / \bar{v}_x , with \bar{v}_x as average velocity in the x -direction; t^* is the dimensionless time, t / t_f , with t_f as the filling time; $(\partial p / \partial x)^*$ is the dimensionless pressure gradient, $(\partial p / \partial x) / [4Q\eta_{T_0} / WH^3]$, with p as the pressure, Q as the flow rate, and η_{T_0} as the initial unreacted mixture viscosity at the initial material temperature, T_0 ; z^* is the dimensionless

transverse direction, $z/(H/2)$; η^* is the dimensionless viscosity

$$\eta^* = \frac{\eta}{\eta_{T_0} \exp(E_\eta^* \{(\Delta T_{ad} - T_0)/(T - \Delta T_{ad})\})}$$

with E_η^* as the dimensionless viscosity activation energy, $E_\eta/R\Delta T_{ad}$, with E_η as the viscosity activation energy and ΔT_{ad} as the adiabatic temperature rise; and Re is the Reynolds number and is defined as:

$$Re = \frac{\rho \bar{v}_x (H/2)}{\eta_{T_0}} \quad (2)$$

where ρ is the density. The dimensionless quantity $(H Re/2L)$ gives the order of magnitude of the accumulation of linear momentum. In general, for typical RIM flow situations (see, e.g. [5])

$$\frac{H Re}{2L} \ll 1$$

Therefore, a steady state of linear momentum can be assumed:

$$\left(\frac{\partial p}{\partial x}\right)^* = \frac{\partial}{\partial z^*} \left(\eta^* \frac{\partial v_x^*}{\partial z^*}\right) \quad (3)$$

The mass balance gives:

$$1 = \int_0^1 v_x^* dz^* \quad (4)$$

Integrating the mass balance by parts using the no slip boundary condition; substituting $(\partial v_x^*/\partial z^*)$ from equation (3), and integrating the resulting expression twice to obtain v_x^* gives [6]

$$v_x^* = \frac{\int_{z^*}^1 (z^*/\eta^*) dz^*}{\int_0^1 ((z^*)^2/\eta^*) dz^*} \quad (5)$$

The pressure drop in the main flow as the mould is being filled can be obtained from the balance of linear momentum, resulting in:

$$\Delta P = \frac{4\eta_{T_0} QL}{H^3 W} \int_0^{(x_f - x_0)/L} \frac{dx^*}{\int_0^1 ((z^*)^2/\eta^*) dz^*} \quad (6)$$

where x_f is the flow front position and x_0 is the length of the flow front region.

With the assumptions given above, the mole balance becomes

$$\frac{\partial C^*}{\partial t^*} + v_x^* \frac{\partial C^*}{\partial x^*} = G k^* (1 - C^*)^2 \quad (7)$$

where C^* is the extent of reaction defined as $(C_0 - C)/C_0$, with C_0 as the initial concentration of reactive species, and C as the concentration of reactive species at time t ; and k^* is the dimensionless reaction rate, $(k/k_{T_m})(C_g^*/(1 - C_g^*)) = (C_g^*/(1 - C_g^*)) \exp(-E^* \{(\Delta T_{ad} - T_m)/(T - \Delta T_{ad})\})$, with k as the kinetic rate constant, k_{T_m} as the kinetic rate constant evaluated at the mean temperature $T_m = (T_0 + T_w)/2$, where T_w is the mould wall temperature, and C_g^* as the gel point conversion. The dimensionless group G , which is called the gelling number, is the most important parameter for the filling step. It is defined as

$$G = \frac{\text{filling time}}{\text{isothermal gel time at } T_m} = \frac{t_f}{t_{g_m}} \quad (8)$$

where the filling time is just the mould volume divided by the volumetric flow rate

$$t_f = \frac{H W L}{Q} = \frac{L}{\bar{v}_x} \quad (9)$$

where \bar{v}_x is the average velocity in the x -direction; and t_{gm} is the time to reach the gel point conversion, C_g^* , at the mean temperature T_m

$$t_{gm} = (k_{T_0} C_0)^{-1} \frac{C_g^*}{1 - C_g^*} \quad (10)$$

where k_{T_0} is the kinetic rate constant evaluated at the initial material temperature. Thus, if the gelling potential is large, considerable chemical reaction will take place during filling. On the contrary, if the gelling potential is small, almost no reaction will occur during the filling step.

The balance of energy reduces to

$$\frac{\partial T^*}{\partial t^*} + v_x^* \frac{\partial T^*}{\partial x^*} = Gz^{-1} \frac{\partial^2 T^*}{\partial z^{*2}} + \frac{Br}{Gz} \eta^* \left(\frac{\partial v_x^*}{\partial z^*} \right)^2 + Gk^*(1 - C^*)^2 \quad (11)$$

the Graetz and Brinkman numbers are defined, respectively, as

$$Gz = \frac{\text{heat transport by convection}}{\text{heat transport by conduction}} = \frac{(\bar{v}_x/L)\rho C_p}{\tilde{k}/(H/2)^2} \quad (12)$$

$$Br = \frac{\text{heat production by viscous dissipation}}{\text{heat transport by conduction}} = \frac{\eta_{T_0}[\bar{v}_x^2/(H/2)^2]}{[\tilde{k}/(H/2)^2]\Delta T_{ad}} \quad (13)$$

where C_p is the heat capacity at constant pressure and \tilde{k} is the thermal conductivity. The temperature was made dimensionless by the adiabatic temperature rise $T^* = (T - T_0)/\Delta T_{ad}$, this way we obtain the same dimensionless group (G) in the reaction term of equations (7) and (11). For a typical RIM situation, the Brinkman number is much smaller than the Graetz number, thus viscous dissipation can be neglected.

Note that in equation (11) the gelling number (G) can also be interpreted as the ratio of heat production by chemical reaction to heat transport by convection.

$$G = \frac{\text{heat production by chemical reaction}}{\text{heat transport by convection}} = \frac{(C_0/t_{gm})H_r}{(\bar{v}_x/L)\rho C_p \Delta T_{ad}} \quad (14)$$

where H_r is the heat of reaction. This definition can be shown to be equivalent to the one given on equation (8) by substituting the adiabatic temperature (ΔT_{ad}) by its value

$$\Delta T_{ad} = \frac{H_r C_0}{\rho C_p} \quad (15)$$

Note that the balance equations are coupled since the viscosity is a function of the extent of reaction and the temperature. They could be decoupled only in special cases. First, if the gelling number is small and the Graetz number is large, the viscosity can be assumed to remain constant during filling and the momentum equation decoupled from the mole and energy balance. Second, if the gelling potential is small but the Graetz number is not large, i.e. there is considerable heat transfer but little reaction during filling, the energy and momentum balance are coupled but they could be decoupled from the mole balance. Lastly, if the gelling number is not small, the three balance equations are coupled. This discussion is illustrated in figure 5.

For the first combination, small G and large Gz , since the flow front can be neglected [6], the simple isothermal plane Poiseuille flow equation can be used to predict the pressure needed to fill the mould. This can be obtained by direct integration of equation (3), using the no slip at the wall and symmetry boundary conditions. The result is

$$\Delta P = \frac{12\eta_{T_0} Q x_f}{H^3 W} \quad (16)$$

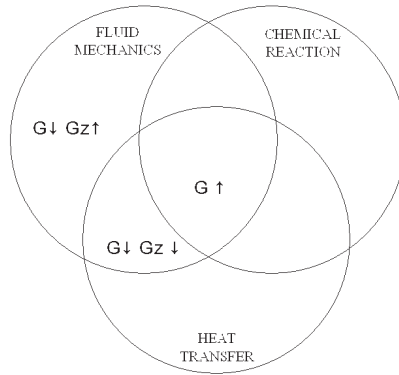


Figure 5. Different phenomena interact at different combinations of the gelling number (G) and the Graetz number (Gz).

where x_f , the flow front position for the case of constant flow rate is simply

$$x_f = \frac{Q}{WH}t \quad (17)$$

Thus, the total pressure needed to fill the mould is

$$\Delta P_f = \frac{12\eta_{T_0}QL}{H^3W} \quad (18)$$

For the other two combinations of G and Gz , the flow front cannot be neglected. The derivation of the model for the flow front can be found in Castro [13]. These coupled phenomena require numerical solutions for which the details are also provided in [13]. Other discussions of filling and curing in RIM, can be found in [14–17].

It is interesting to note that, qualitatively examining the influence of the gelling potential and the Graetz number on the pressure rise, one is able to obtain valuable information about the degree of coupling of different phenomena and to find ways to deal with each situation. In the instance described previously (low G and large Gz), the viscosity will remain nearly constant during filling and the pressure rise is given by equation (16), which predicts a linear increase in pressure with filling time. Second, if G is small, but Gz is not large, the pressure rise will be lower than the one predicted using a constant viscosity (η_{T_0}), if the wall temperature is larger than the initial material temperature (typical RIM case); and higher if it is the other way around ($T_0 > T_w$). This is due to heat conduction to or from the walls, since the viscosity decreases with increasing temperature. If $T_w > T_0$, the walls act as a heat source and when $T_0 > T_w$ as a heat sink. Lastly, if the gelling number is large, the pressure rise will be larger than the one predicted assuming constant viscosity (η_{T_0}). It may rise so high as to result in a short shot. These four cases are sketched in figure 6.

For most typical RIM cases, the gelling potential G is low and the chemical reaction can be neglected during filling. Thus, for a rectangular part, the fill pressure can be predicted by equation (16). This example shows how by analysing the physical phenomena using the information obtained through scaling analysis, modelling can be greatly simplified. In the following section, the focus shifts to empirical modelling and different cases are presented to illustrate its use.

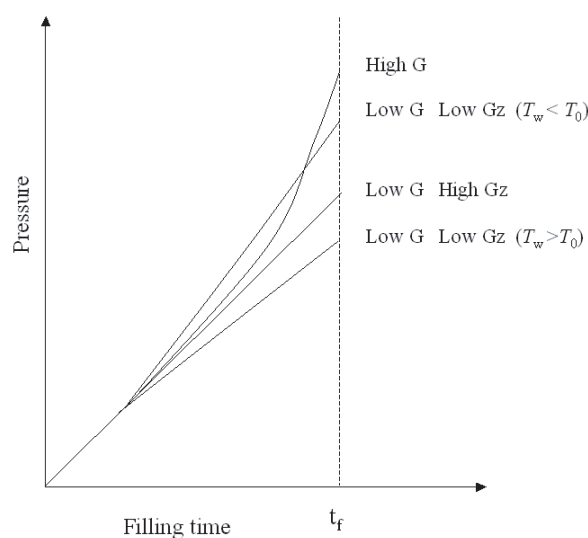


Figure 6. Influence of the gelling number (G) and Graetz number (Gz) on the pressure rise.

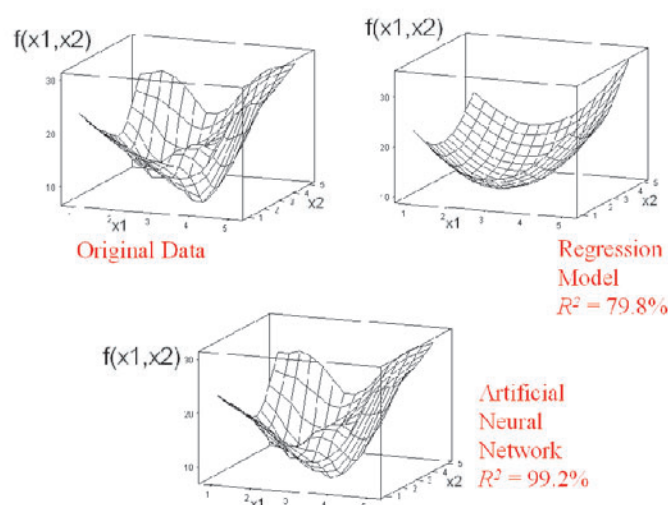


Figure 7. An original function approximated using a regression model and an ANN.

3. Empirical models

Empirical models are mathematical approximations of inherent simplicity that, as explained previously, are not based on physical or chemical principles. ‘Data fitting’, ‘meta-modelling’, or ‘response surface’ are other names that have been used to refer to this area.

There are many functional forms that the empirical models can take. Ranging from the linear regression model to the artificial neural network (ANN), to date there is no strict way to select the most appropriate one for an application. Figure 7 shows how different results can be when using different empirical models in terms of the approximation quality.

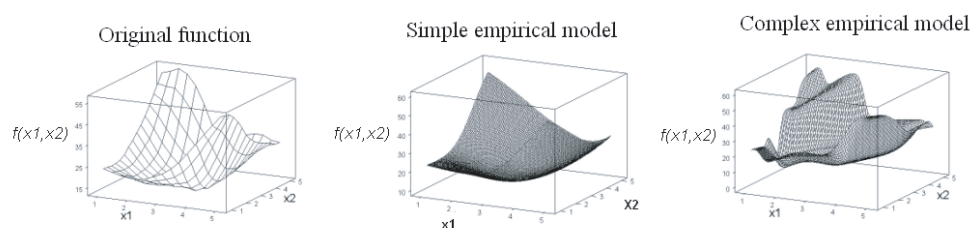


Figure 8. Original function approximated with a simple empirical model (fewer fitting parameters) and a complex empirical model (several fitting parameters).

The goodness-of-fit of an empirical model also has many different forms. Shown in figure 7 is the R^2 value, formally known as the coefficient of determination, which ranges from 0% to 100% and measures how close the model approximates the original function or data (100% implies a perfect fit). The use of the mean absolute error (MAE) and the mean absolute per cent error (MAPE) are also popular measures. The equations for these measures are as follows:

$$\text{MAPE} = \frac{100}{n} \sum_{i=1}^n \left| \frac{y_i - \hat{y}_i}{y_i} \right| \quad (19)$$

$$\text{MAE} = \frac{100}{n} \sum_{i=1}^n |y_i - \hat{y}_i| \quad (20)$$

$$R^2 = 1 - \frac{\sum_{i=1}^n (y_i - \hat{y}_i)^2}{\sum_{i=1}^n y_i^2 - (1/n)(\sum_{i=1}^n y_i)^2} \quad (21)$$

where n is the number of experimental points, y_i and \hat{y}_i are the experimental response and the prediction at the i th experimental point, respectively.

In general, when empirical models are applied, it is recommended to start by using the simplest possible model (i.e. the one with the lowest number of parameters), and improving the fit by trying gradually more complex models. This practice has to do with the fact that, if an extremely complicated model is used from the beginning, this model might fit the experimental data perfectly but might not be smooth between these experimental points (i.e. it does not predict well). Figure 8 shows graphically the effects of having an unnecessarily complex model. Another popular way to prevent the deterioration of an empirical model's prediction capability, referred to as 'overfitting', is to partition the number of data points available to fit a model in two disjoint sets. The first set is used to fit the model, and the second set to test its prediction capabilities. The second set is commonly known as the 'validation set' and can be evaluated with the measures detailed in equations (19)–(21) among others.

In order to demonstrate the use of empirical models, a series of case studies are presented next in which modelling and simulation have been used to elicit proper settings of process and/or design parameters in reactive polymer processing applications. These case studies were selected to provide instances where empirical modelling plays a critical role when used along with data generated through experiments, computer simulations, and through physics and chemistry based models. The ultimate goals of these cases were optimization oriented. In this section, they are presented mainly to discuss their empirical modelling applications. Optimization is discussed later in this paper.

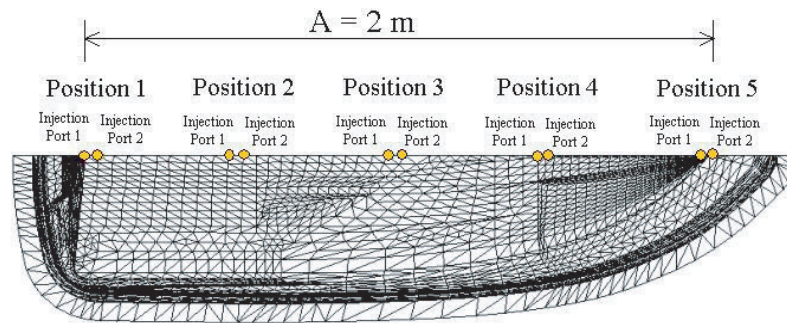


Figure 9. Finite element analysis (FEA) mesh of half a boat hull. Circles represent the sampling positions for the two injection ports along the A dimension of the bottom of the boat hull.

4. Location of two in-mould coating injection ports

Fibreglass reinforced polyester (FRP) parts compression moulded from SMC are prone to surface defects such as porosity and sinks [18–21]. Even though it appears that some of these defects can be eliminated by techniques such as vacuum moulding, with current SMC the resulting surface is not yet consistently up to automotive standards for exterior automotive body panels. In-mould coating (IMC) is a single-component product designed to enhance the surface of FRP mouldings in functional and cosmetic properties [22]. IMC is a reactive fluid, which when injected onto a cured SMC part, cures and bonds to provide a paint-like coating to the part surface. As a result, today IMC is considered an integral part of the moulding cycle when producing compression moulded SMC exterior automotive body panels. One of the keys to the success of the process is to locate the injection gate optimally with the objective to minimize or eliminate the potential for trapping air in the appearance section of the part.

Let us consider the half-hull of a boat with uniform thickness shown schematically in figure 9. It is required to in-mould coat the boat hull using two injection ports. The use of multiple injection ports is considered necessary for certain applications where the injection capacity of one IMC unit might not suffice to completely coat the part. Referring to figure 9, the two injection ports must be located at the bottom of the hull along the dimension A ($A = 2$ m). The reason behind limiting the location of the injection ports to the bottom of the boat has to do with the cosmetic appeal that the finished part must have: the place where IMC is injected will, in most cases, leave a mark; this is the typical case in the industry [18, 22].

It can be shown that for typical conditions, the chemical reaction can be neglected during filling. This greatly reduces the simulation effort needed to predict the fill pattern [2]. Two quality PMs were chosen for minimization:

$$t_{\text{diff}} = t_{\text{fill}} - t_{\text{touch}} \quad (22)$$

$$t_{\text{kmit}} = t(\text{kmit line}) \quad (23)$$

Equation (22) measures the difference between the time it takes to completely fill the mould cavity (t_{fill}) and the time at which the first flow front touches the exterior edge of the part (t_{touch}). This equation provides a measure of the uniformity of the coating spread. The measure t_{kmit} (equation (23)) is defined as the time at which the two flow fronts (one from each nozzle) meet and form a knit line. Contrary to thermoplastic IM, knit lines in IMC are not a problem unless they occur near the end of fill [18, 22]. Criteria such as the ones defined here have been used successfully to select injection nozzle location for industrial moulds [18, 22, 23].

In order to take advantage of the symmetry of the hull, a finite element analysis (FEA) mesh of half of the boat was created. The FEA mesh was then used in conjunction with simulation software (MoldflowTM [25]) to obtain predictions of the flow pattern and therefore for equations (22) and (23) at different combinations of positions of both injection ports. In the ideal situation in which there are large amounts of resources such as computational power, time, and money; it is possible to try several position combinations for the injection nozzles to find a suitable one according to equations (22) and (23). However, if this is not the case, empirical models can be used to generate estimates for these PMs instead of running a large number of computer simulations. Furthermore, these models can become part of an optimization problem to find the best location combination in a more convenient manner.

Two variables $\{x_1, x_2\}$ were defined, where x_j denoted the position of the j th injection port, $j = 1, 2$, along the dimension A on the bottom of the hull of the boat (figure 9). Each of these variables was sampled at five different positions. The positions for x_1 were $\{0.00, 0.46, 0.94, 1.41, 1.95\}$ m, and for x_2 were $\{0.05, 0.52, 1.05, 1.51, 2.00\}$ m.

The factorial combination of the two position variables $\{x_1, x_2\}$ at five levels each resulted in an experimental design with 25 simulation runs. From each simulation, the predicted values for t_{fill} , t_{touch} , and t_{knit} were measured. Because optimization through DEA was the final goal of this study, and the application of this technique required a large number of predictions for equations (22) and (23) it was necessary to use empirical models. Two types of empirical models used in this case are explained below: linear regression models and ANNs.

Regression analysis [26–29] is a widely used empirical modelling technique from which a second-order polynomial approximation can be obtained, resulting in the expression:

$$\hat{y} = \hat{\beta}_0 + \sum_{i=1}^k \hat{\beta}_i x_i + \sum_{i=1}^k \hat{\beta}_{ii} x_i^2 + \sum_{i=1}^{k-1} \sum_{j>i}^k \hat{\beta}_{ij} x_i x_j \quad (24)$$

where \hat{y} is the predicted response (dependent variable), x_i is the i th independent variable out of the k existing ones, and the $\hat{\beta}$ parameters are the estimated regression coefficients obtained by least squares reduction.

Another powerful meta-modelling technique is the use of an ANN. An ANN is an information-processing system where processing occurs at many simple elements called neurons organized in layers and where signals are passed between neurons over connection links. Each connection link has an associated weight that multiplies the signal transmitted and each neuron applies an activation function to its net input (sum of weighted input signals) to determine its output signal [30]. Figure 10 shows the structure of a widely used ANN [31–34]. This ANN has one input layer with k neurons to process the k independent variables, one hidden layer with m neurons, and one output layer with r neurons to provide the r responses. Two layers of weights are also present in this ANN. The first modifies the information transmitted from the input layer to the hidden layer, and the second, the information transmitted from the hidden layer to the output layer. The mathematical expression of the ANN model with one input layer, one hidden layer, and one output layer is given by

$$\hat{Y} = \Phi(\hat{W}_2^T \Psi(\hat{W}_1 X + \hat{b}_1) + \hat{b}_2) \quad (25)$$

where \hat{Y} is the vector of predicted responses, X is the vector of inputs, \hat{W}_1 is a matrix containing the weights on the connection links between the input layer and the hidden layer, and \hat{W}_2^T is the transpose of \hat{W}_2 , which is a matrix containing the weights for the links between the hidden layer and the output layer; \hat{b}_1 and \hat{b}_2 are vectors containing a special type of weights called biases that modify the net input for the hidden layer and the output layer, respectively; Ψ is the activation function of the neurons of the hidden layer, and Φ is the activation function of

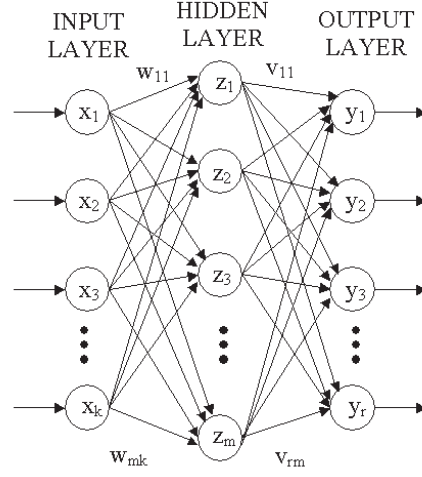


Figure 10. Backpropagation ANN with one hidden layer with m neurons, two layers of weights, k inputs, and r outputs.

the neurons in the output layer. Obtaining the weights in \hat{W}_1 , \hat{W}_2 , \hat{b}_1 , and \hat{b}_2 is commonly done with the backpropagation algorithm [34], which is in essence similar to a least squares reduction.

For the boat application, expressions for t_{diff} and t_{knt} as functions of $\{x_1, x_2\}$ were both obtained first by regression analysis and then by fitting ANNs of the form described in equation (25). The ANN used to fit t_{diff} had six neurons in the hidden layer, while the ANN used to fit t_{knt} had two neurons. In both cases, the inputs and outputs were scaled to fall in the range $[-1, 1]$, and in both cases the neurons in the hidden layer used equation (26) as the activation function, and the neurons in the output layer used equation (27).

$$\Psi(x) = \frac{e^x - e^{-x}}{e^x + e^{-x}} \quad (26)$$

$$\Phi(x) = x \quad (27)$$

A comparison between the surface plots of the original data for t_{diff} , the approximation by regression analysis, and the approximation by ANN is presented in figure 11. A similar comparison for t_{knt} is presented in figure 12. These figures visually show the approximation capabilities of the ANNs, as well as their superiority over the quadratic approximations from regression analysis in this particular case. In figures 11 and 12, the R^2 values obtained for each approximation are also reported to facilitate the comparison. A key to successfully fit the ANNs was to keep a validation set to test the prediction capabilities of the meta-model. Meta-models that are accurate to a high degree increase the confidence of an optimization procedure. Tables 1 and 2 show the parameters for ANN meta-models \hat{t}_{diff} and \hat{t}_{knt} , respectively.

Several qualities make ANNs attractive for meta-modelling in polymer processes. First, although the fitting of the neural network by backpropagation can be slow, once fitted the neural network can produce its output very rapidly. ANNs also have been shown to provide good approximations in presence of noisy data and small number of experimental points [35]. Furthermore, the assumptions under which ANNs work are less strict than those for regression meta-models.

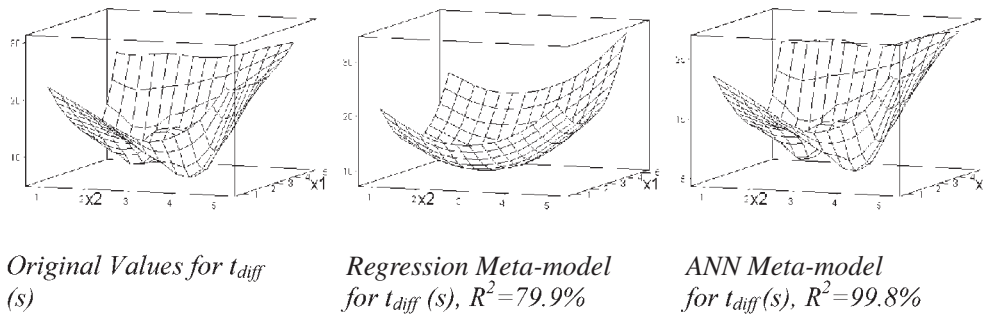


Figure 11. Comparison of meta-models fit to the original values of t_{diff} .

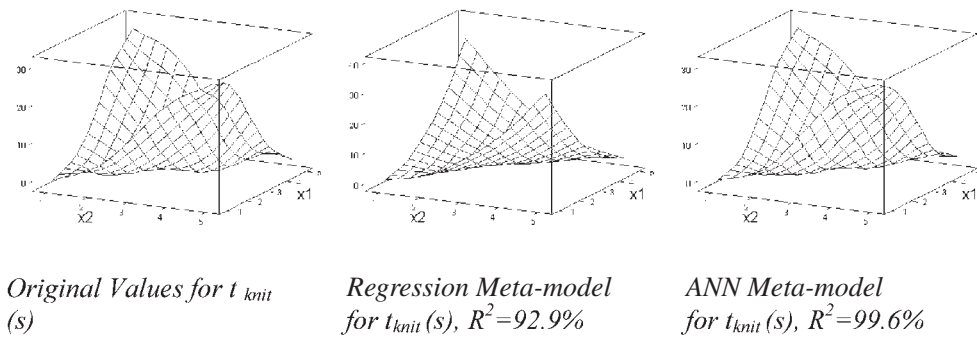


Figure 12. Comparison of meta-models fit to the original values of t_{knit} .

Table 1. Weights for the ANN meta-model for t_{diff} .

Weights from input layer to hidden layer \hat{W}_1	Biases for hidden layer \hat{b}_1	Weights from hidden layer to output layer \hat{W}_2	Bias for output layer \hat{b}_2
-2.8058	3.4722	4.8828	-0.9413
3.6816	0.3287	-1.3445	-0.8393
-1.5861	-1.0482	1.0135	-2.5725
-1.1412	-3.0699	1.0923	0.6796
-1.4799	-1.0969	-1.8667	0.8320
3.0538	-5.0666	6.0859	-1.1879

Table 2. Weights for the ANN for t_{knit} .

Weights from input layer bias for hidden layer to hidden layer \hat{W}_1		Weights from hidden layer to output layer \hat{W}_2		Bias for output layer \hat{b}_2
-1.4609	1.5503	-1.5357	1.1402	1.1335
1.4762	-1.4016	-1.6418	1.1555	

This first case study exemplified how simulation and modelling can be coordinated to speed up the analysis required for *a posteriori* optimization procedure. Special emphasis is given here to the selection of models based on goodness-of-fit and being careful not to deteriorate the ability of the model to make predictions by keeping a validation set.

5. Production of in-mould coated SMC parts

This second case retakes the IMC application to SMC production. The focus here, however, is on the analysis of the combined process (SMC compression moulding + IMC injection). Key PMs are cycle time, part surface quality, and part dimensional consistency. This case demonstrates the possibilities of using physics based models and empirical models in a coordinated manner.

The typical SMC used for automotive exterior body panels consists of polyester resin, filler, glass fibres, initiator, inhibitor, and other additives. Once the automotive or truck manufacturer has approved the SMC composition, the moulder has the freedom to adjust, within given specifications, the formulation contents of only three components: filler, inhibitor, and initiator. Adjusting the contents of these components can be done with the purpose of minimizing the cycle time and improving the surface flatness and the overall part quality. Additionally, the moulder can adjust the moulding temperature as part of the processing conditions. The role of the temperature is critical in reactive polymer processes such as SMC and IMC, where it impacts all of the most important phenomena involved: rheology, chemical reaction, and heat transfer. Regarding the IMC, the choice of inhibitors and initiators will affect the cycle time.

The fact that to date there is no model to predict surface quality requires the use of a surrogate measure instead. In this case, the Ashland Index, an industrially accepted measure, is used. The Ashland Index measures the surface waviness of a part [36]: the lower the index value, the lower the surface waviness, and the higher the surface quality. The dependence of the Ashland Index on the controllable variables is necessarily determined by means of experimentation. The same is true for dimensional consistency for which it is necessary to obtain experimental measures of the deviation from the desired part dimension, length in this case; create an empirical model to map the functionality of this measures to the controllable variables, and then to compute the rate of change of this function w.r.t. the controllable variables. This process will be explained later in this section.

Figure 13 shows a schematic representation of the elements and variables involved in the cycle time of the SMC/IMC system as they relate to an optimization problem. The labels in the leftmost area of this figure indicate the nature of the items that are displayed at each level of the figure (to the right of each label). The SMC part under consideration is a rectangular part of dimensions W , L , and h (width, length, and thickness, respectively). The part dimensions and the initial SMC temperature (T_0) do not change during the analysis of this case, i.e. they are considered constant. The controllable variables are: (1) mould wall temperature (T_w), (2) SMC filler content (F), (3) initial inhibitor concentration for SMC (C_{Z0s}), (4) initial initiator concentration for SMC (C_{I0s}), (5) initial inhibitor concentration for IMC (C_{Z0i}), and (6) initial initiator concentration for IMC (C_{I0i}). These controllable variables can be systematically set to discrete values to measure several responses either by using a physics based model or by running an experiment. The responses of interest for this case are: (1) fill time of SMC (t_{fs}), (2) inhibition time of SMC (t_{zs}), (3) cure time of SMC (t_{cs}), (4) Ashland Index (A_I), (5) length difference of the cold SMC part and the cold mould (L_{diff}), (6) inhibition time of IMC (t_{zi}), (7) cure time of IMC (t_{ci}), and (8) fill time of IMC (t_{fi}). These measures are then used to obtain the empirical expressions or meta-models $\{\hat{t}_{fs}, \hat{t}_{zs}, \hat{t}_{cs}, \hat{A}_I, \hat{L}_{diff}, \hat{t}_{zi}, \hat{t}_{ci}\}$ that provide the estimates necessary for an optimization problem. The model of the fill time for IMC is simple enough as to be able to be used directly to obtain quick estimates; therefore no meta-model is required to replace it. The optimization problem then becomes, in other words, to set the controllable variables to minimize the cycle time, minimize the Ashland Index (and thereby maximize the surface quality), and minimize the rate of change of \hat{L}_{diff} w.r.t. the mould temperature and to

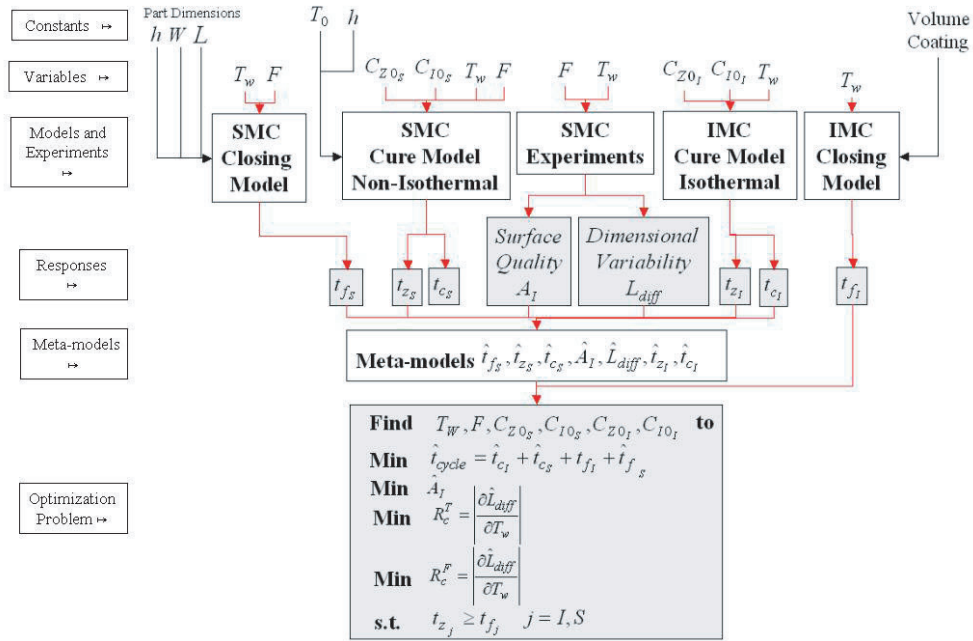


Figure 13. Schematic representation of the elements and variables involved in the optimization of the SMC/IMC system for appearance parts. F stands for SMC filler contents (as weight per cent of the total), T_0 is the initial temperature of the SMC charge, T_w is the temperature of the mould, h, L, W are the final thickness, length, and width of the SMC part, respectively, C_{I0_s} is the initial initiator concentration for the SMC, C_{I0_I} is the initial initiator concentration for the IMC, C_{Z0_s} is the initial inhibitor concentration for the SMC, C_{Z0_I} is the initial inhibitor concentration for the IMC, t_{z_s} is the inhibition time of the SMC, t_{z_I} is the inhibition time of the IMC, t_{c_s} is the cure time of the SMC, t_{c_I} is the cure time of the IMC, t_{f_s} is the fill time of the SMC, and t_{f_I} the fill time of the IMC.

the SMC filler content (and thereby maximize the dimensional consistency), while allowing enough inhibition time for the SMC to fill the mould.

The SMC/IMC process can be effectively evaluated by many PMs; cycle time, surface quality, and dimensional consistency are considered among the most important and it is necessary to consider them simultaneously because many possible compromises might arise between them. These three PMs depend on several variables; however, in this case the interest is to map their dependence on a total of six controllable variables: $\{T_w, F, C_{Z0_s}, C_{I0_s}, C_{Z0_I}, C_{I0_I}\}$ within certain experimental region. The case here described involves the manufacture of a rectangular SMC part with length $L = 0.7112$ m (28 in), width $W = 0.6096$ m (24 in), and thickness $h = 2.54 \times 10^{-3}$ m (0.1 in). The initial temperature of the SMC (T_0) and the available press tonnage (F_p) are considered to be 298.15 K (25°C) and 100 tnf, respectively, throughout this case. Further, the IMC volume for such part is calculated using a final coating thickness of 0.003 in, resulting in a volume of 2.016 in³.

The first PM, cycle time (t_{cycle}), is the total time that the mould is seized: the sum of the time it takes to completely fill the mould and the time it takes to cure the material for both the SMC and IMC. This relationship has the following dependence:

$$t_{cycle} = t_{f_s}(T_w, F_p, L, W, h) + t_{c_s}(T_w, F, C_{Z0_s}, C_{I0_s}, T_0, h) + t_{f_I}(T_w, L, W, h_I) + t_{c_I}(T_w, C_{Z0_I}, C_{I0_I}) \quad (28)$$

Alternatively, t_{cycle} can be represented as the addition of the cycle time of the SMC process ($t_{\text{cycle}}^{\text{S}}$) and the IMC process ($t_{\text{cycle}}^{\text{I}}$), where each cycle time results from adding the fill time and cure time of each process.

The second PM, surface quality is measured by means of the Ashland Index (A_I) [36], which measures the surface waviness of a part, and therefore is an indirect measure of surface quality. A_I can be shown to have the following functionality [37]:

$$A_I = f(T_w, F) \quad (29)$$

In this case we will assume that the IMC process does not affect the A_I of the substrate.

The third PM, dimensional consistency is defined here as the sensitivity of the part dimensions to variations in the moulding temperature and the SMC filler content. To elicit this measure, first an experiment was performed where T_w and F were systematically varied to determine the length variation of the SMC part w.r.t. the mould:

$$L_{\text{diff}} = L_{\text{cp}} - L_{\text{cm}} \quad (30)$$

where L_{cp} is the length of the cold SMC part, and L_{cm} is the length of the cold mould, and L_{diff} is a variation of an industrially accepted measure for part shrinkage. The values of L_{diff} were then used to obtain a meta-model of this measure, \hat{L}_{diff} , as a function of T_w and F . Finally, the surrogates for dimensional consistency could then be obtained from \hat{L}_{diff} as follows:

$$R_c^T = \left| \frac{\partial \hat{L}_{\text{diff}}}{\partial T_w} \right| \quad (31)$$

$$R_c^F = \left| \frac{\partial \hat{L}_{\text{diff}}}{\partial F} \right| \quad (32)$$

where R_c^T and R_c^F stand for rate of change w.r.t. mould temperature and filler, respectively. These surrogate measures will be the indicators for dimensional consistency.

In this project, a mechanistic kinetic model was used to independently represent the reaction rate of both components, SMC and IMC. This model was developed by Stevenson [38] and simplified by Lee [39], and is based on the free radical polymerization mechanism.

Under suitable assumptions the equations of the model are as follows [38] (in the following explanation, the use of sub-indices S and I to represent SMC and IMC, respectively, has been omitted to keep it general):

- (1) The initiator (I) decomposes to give free radicals (R^\cdot).



$$\frac{-dC_I}{dt} = k_d C_I \quad (34)$$

- (2) At time t_z (inhibition time), we have

$$2(C_{I0} - C_I(t_z)) = C_{z0} \quad (35)$$

where C_{I0} represents the initial initiator concentration, $C_I(t_z)$ is the initiator concentration at time t_z and C_{z0} is the initial inhibitor concentration.

- (3) For times larger than t_z , there are free radicals available to react with monomers and generate heat:



$$\frac{-dC_M}{dt} = k_p C_M C_{R^\cdot} \quad (37)$$

where C_M represents the monomer concentration, and C_R the concentration of free radicals, which is given by

$$C_R = 2(C_{I0} - C_I(t)) - C_{z0} \quad (38)$$

Both k_d and k_p are assumed to be equations of the Arrhenius type, expressed as:

$$k_d = k_{d0} e^{-E_d/RT} \quad k_p = k_{p0} e^{-E_p/RT} \quad (39)$$

The kinetic parameters characterizing the model, i.e. k_{d0} , E_d , k_{p0} , and E_p , are obtained from differential scanning calorimeter (DSC) measurements as explained by Lee [39] and Stevenson [38]. The values to use this model for SMC were obtained by Castro and Lee [40] and the values for IMC can be found in [41].

In the case of the SMC, curing involves a balance between heat conduction (primarily across the thickness of the part) and heat generated by the curing reaction. For simplicity, the balance is restricted to a simple one-dimensional heat transfer model with mould walls at constant temperature. The temperature balance described here is given by

$$\rho C_p \frac{\partial T}{\partial t} = k \frac{\partial^2 T}{\partial z^2} + H_r \frac{\partial C^*}{\partial t} \quad (40)$$

where z represents the coordinate perpendicular to the mould surfaces, ρ is the density, C_p is the specific heat, k is the thermal conductivity, H_r is the heat of reaction, and $\partial C^*/\partial t$, the reaction rate, is given by equation (34) with the monomer conversion, C^* , defined as follows:

$$C^* = \frac{C_{M0} - C_M}{C_{M0}} \quad (41)$$

where C_{M0} is the initial amount of monomer and C_M represents the (instantaneous) monomer concentration.

Differential equations (34), (37), and (40) can be solved by using the finite differences method, as shown in Castro and Lee [40]. A sample of the output of this model is shown in figure 14, where the extent of reaction is given as a function of time for four SMC locations. The inhibition time, t_z , is identified as the earliest time at which the extent of reaction became non-zero, and the cure time is the latest time when the extent of reaction became larger than 90%.

In the case of IMC, since we can assume isothermal at the mould wall temperature due to the small coat thickness [41], only the solution to equation (37) is required, and the inhibition time is given by the expression:

$$\ln t_z = \ln \left[\frac{-1}{k_{d0}} \ln \left(1 - \frac{C_{z0}}{2C_{I0}} \right) \right] + \frac{E_d}{RT} \quad (42)$$

The fill time of the SMC is obtained by iteratively solving the following expression developed by Abrams and Castro [42, 43] for the time at which the instantaneous gap is equal to the final thickness:

$$F_c = \frac{4\eta V U(t)}{h(t)^2} + \frac{2m U(t)^n V^{n+2}}{\delta^n W^{n+1} h(t)^{2n+3} 2^{n+1} (n+2)} \quad (43)$$

In this model, F_c is the (given) press tonnage, η is the SMC resistance to extension, V is the part volume, $U(t)$ is the instantaneous closing speed, $h(t)$ is the instantaneous gap, m is the power law consistency index, n is the power law index, and δ is the thickness of the lubricating layer [42]. The parameters used for this model can be found in [43]. A sample of the output of this model is shown in figure 15.

The fill time of the IMC is estimated by the model proposed by Castro and Griffith [18]:

$$t_{fi} = \frac{K^{1/n} (1/n+2) V^{(n+3)/2n} 2^{(n+3)/2n}}{F_c^{1/n} (n+3)^{1/n} \pi^{(n+1)/2n} (3n+5)} (2n) \left(\frac{1}{h_{f2}^{(3n+5)/2n} - h_{f1}^{(3n+5)/2n}} \right) \quad (44)$$

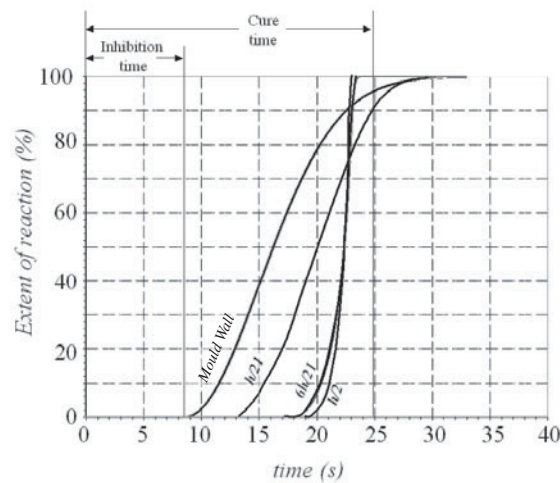


Figure 14. Sample output of the kinetic mechanistic model to predict inhibition and cure times in SMC. The different curves correspond to the extent of reaction at different points along the thickness (h) of the SMC part.

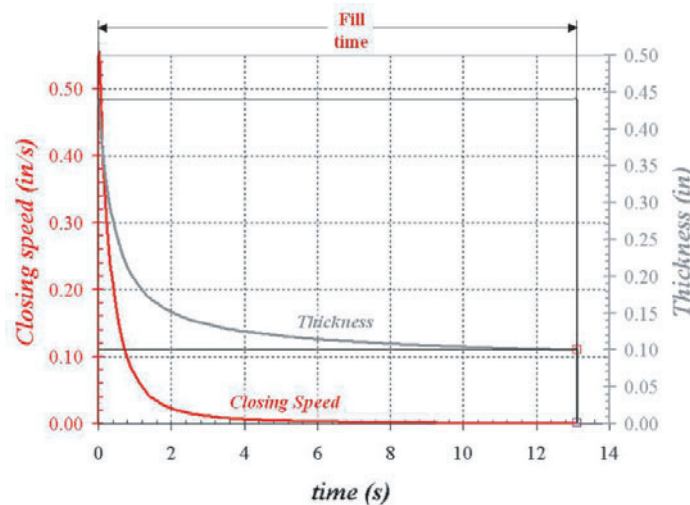


Figure 15. Sample output of the model to predict the fill time of SMC.

where K is a function of the temperature of the mould given as $K = 14.287 e^{800/T_w}$, n is the power law index ($n = 0.315$ for IMC), V is the volume of the coating, F_c is the given press tonnage, h_{f1} is the initial thickness of the IMC pool ($h_{f1} = 0.03$ in), and h_{f2} is the final IMC thickness. Because most of the variables are given specific values to model the IMC, equation (44) reduces to a simple expression where the only variable is T_w , making it convenient to obtain quick estimates from this model.

The models described so far, with exception of equation (44), are complicated enough to require the use of empirical models to obtain estimates in a more convenient manner. Further, since no physics based models are available to represent the required functionality for A_I and L_{diff} , the use of empirical models is a necessity for these two responses. Experimental designs were used to measure A_I and L_{diff} , respectively, at different levels of T_w and F [3]. The designs

are full factorials with both variables at three levels each with five replicates under each of the nine experimental conditions.

Full factorial designs were also used to obtain estimates for t_{zs} and t_{cs} , as functions of T_w , F , C_{Z0s} , and C_{I0s} , and t_{fs} as a function of T_w and F . The complete design had 81 runs (four variables at three levels each). Similarly, estimates for t_{zi} and t_{ci} , as functions of T_w , C_{Z0i} , were obtained through the same type of experimental design [1]. It was not necessary to generate a data set for t_{fi} because, as it was explained before, it was considered that the model was capable of providing estimates fast enough for an optimization task.

The data sets generated in the previous step were used to fit meta-models that would (1) take the place of the SMC closing model, the SMC non-isothermal cure model, and the IMC isothermal cure model, or (2) that would model the functionality in the experimental sets (A_I and L_{diff}). The strategy followed to fit the meta-models was to start with a simple model, i.e. a regression model, and if the fit was not good enough, proceed to fit a more complicated model, i.e. an ANN, for which a progressive addition of hidden neurons indicated increasing complexity of the desired response surface. The meta-model used to approximate t_{fs} was of the regression type, and achieved a R^2 value of approximately 100% when the independent variables, T_w and F , were scaled to fall within the range $[-1, 1]$. The expression is as follows:

$$\hat{t}_{fs} = -0.1780 - 0.0425T_w + 0.9545F - 0.0055T_w^2 + 0.1665F^2 - 0.0180T_w \cdot F \quad (45)$$

The values of t_{zs} followed the same scheme of transformations described for t_{fs} , however, for this response the use of an ANN yielded a better fit ($R^2 = 99.6\%$) when compared to the simpler regression model ($R^2 = 96.6\%$). The ANN used to fit t_{zs} needed only two neurons in the hidden layer, so the resulting model is not very complex. The ANN is summarized by the equation:

$$t_{zs} = \Phi \left([-0.6405 \quad -0.5694] \right. \\ \left. \times \Psi \left(\begin{bmatrix} 0.5989 & 0.0010 & -0.3965 & 0.3710 \\ 1.8227 & -0.0010 & -1.0209 & 1.8806 \end{bmatrix} \begin{bmatrix} T_w \\ F \\ C_{Z0} \\ C_{I0} \end{bmatrix} + \begin{bmatrix} 0.7155 \\ 3.8828 \end{bmatrix} \right) + 0.2273 \right) \quad (46)$$

where Φ and Ψ are functions of the forms defined in equations (27) and (26), respectively.

The SMC cycle time, t_{cycle}^S , which is the addition of t_{fs} and t_{cs} , is fitted by an ANN with two neurons in the hidden layer, following the same transformations as in the two previous meta-models. The fit results in a R^2 value of 99.6%, while using a regression model would have yielded 98.1%. This ANN is described by the equation:

$$t_{cycle}^S = \Phi \left([-1.4459 \quad 0.9615] \right. \\ \left. \times \Psi \left(\begin{bmatrix} 0.7523 & 0.0299 & -0.2988 & 0.6762 \\ -0.2589 & 0.1576 & 0.0766 & -0.0843 \end{bmatrix} \begin{bmatrix} T_w \\ F \\ C_{Z0} \\ C_{I0} \end{bmatrix} + \begin{bmatrix} 1.9018 \\ -0.5246 \end{bmatrix} \right) + 1.2227 \right) \quad (47)$$

with Φ and Ψ as described by equations (30) and (29), respectively.

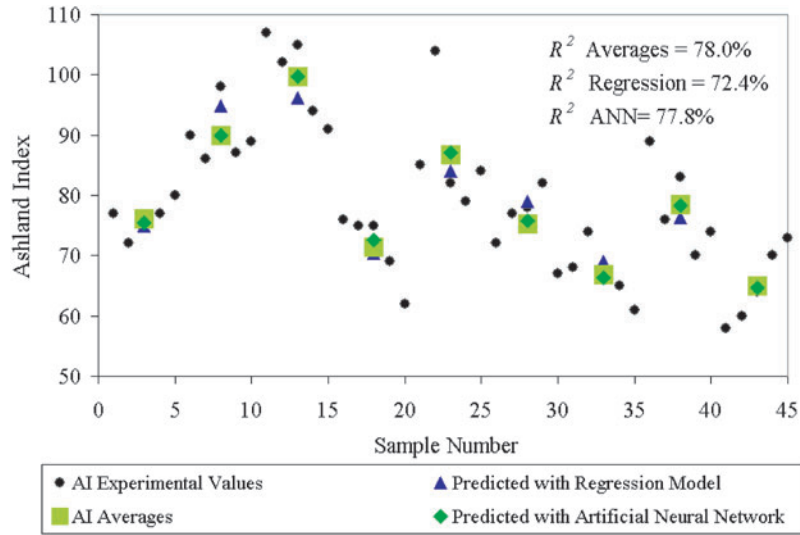


Figure 16. Comparison between the fit obtained via regression analysis and ANN for experimental values of A_1 .

The experimental values obtained for A_1 were used to fit an ANN that achieved an R^2 of 77.8% with two neurons in the hidden layer. The reason why this is considered to be a good fit has to do with the fact that for each of the nine available experimental conditions tested (each condition is a combination of specific values of F and T_w) there are five measurements (replicates). By examining figure 16, one can see that the measurements for A_1 are dissimilar to each other. This is the random variation of the process that involves noise variables and controllable variables that were not included in the study. Because the idea is to find and use a deterministic model, every time that one inputs the combination (F^*, T_w^*) , the prediction for A_1 using this model will be the same. Therefore, this prediction could match at most one of the experimental values (assuming that the replicates are all different). In such a case, most typical statistical models try to fit a surface that is as close as possible to the average of these replicates under normality assumptions, since the average minimizes the distance to all replicates. With this in mind, if the averages were used to predict each of the experimental points of A_1 in figure 16, the R^2 value obtained would be 78%. Using this value as a reference, the ANN meta-model (at $R^2 = 77.8\%$) does a comparatively good job of fitting the experimental A_1 points. Had a regression model been used, it would have achieved a value of $R^2 = 72.4\%$. Figure 16 shows a comparison of the predictions by the different meta-models to the experimental points for A_1 , all of them plotted against the experimental order. Notice however that A_1 is not a function of the run number, but a function of F and T_w . Figure 16 shows how the ANN approximate the data averages better than the regression model for this case.

The ANN for A_1 takes the following form:

$$\hat{A}_1 = \Phi \left([2683.7 \quad 2683.2] \Psi \left(\begin{bmatrix} -0.3823 & -3.143 \\ 0.3823 & 9.982 \end{bmatrix} \begin{bmatrix} F \\ T_w \end{bmatrix} + \begin{bmatrix} 0.3394 \\ -0.7336 \end{bmatrix} \right) - 0.6560 \right) \quad (48)$$

with Φ and Ψ as described by equations (27) and (26), respectively.

Following the same transformation scheme as in the A_1 values, an ANN was fitted to the experimental values of L_{diff} . In this case, the regression model provided a fit that was close

enough to what the averaged values would have given. The R^2 value for the regression model was of 95%, while the averaged values would have given a value of 95.5%, and an ANN a value of 95.5%. Adding to the decision to keep the regression meta-model is the form of the PMs defined by equations (31) and (32). These PMs involve the partial derivatives of L_{diff} w.r.t. F and T_w , the computation of which becomes simpler when working with a polynomial expression.

The meta-model for L_{diff} is, then:

$$\hat{L}_{\text{diff}} = -0.4122 + 0.2437F - 0.4407T_w + 0.0889F^2 + 0.1840T_w^2 + 0.0389F \cdot T_w \quad (49)$$

The first partial derivative of \hat{L}_{diff} w.r.t. T_w then becomes:

$$\frac{\partial \hat{L}_{\text{diff}}}{\partial T_w} = \hat{\beta}_2 + 2\hat{\beta}_{22}T_w + \hat{\beta}_{12}F = -0.4407 + 0.368T_w + 0.0389F \quad (50)$$

where $\hat{\beta}_2$, $\hat{\beta}_{22}$, and $\hat{\beta}_{12}$ are the regression coefficients for T_w , T_w^2 , and $F \cdot T_w$ in equation (49).

Similarly, the first partial derivative of \hat{L}_{diff} w.r.t. F is:

$$\frac{\partial \hat{L}_{\text{diff}}}{\partial F} = \hat{\beta}_1 + 2\hat{\beta}_{11}F + \hat{\beta}_{12} = 0.2437 + 0.1778F + 0.0389T_w \quad (51)$$

where $\hat{\beta}_1$, $\hat{\beta}_{11}$, and $\hat{\beta}_{12}$ are the regression coefficients for F , F^2 , and $F \cdot T_w$, respectively, in equation (49).

Regarding the IMC process, the first meta-model approximates \hat{t}_{z1} as a function of T_w , C_{101} , and C_{Z01} . The values for the independent variables as well as the response are scaled to fall within the range $[-1, 1]$. A regression model gave a R^2 value of 98.4%, thus it was decided to keep this approximation. The meta-model is as follows:

$$\begin{aligned} \hat{t}_{z1} = & -0.7036 - 0.1478T_w - 0.4083C_{101} + 0.3257C_{Z01} + 0.0250T_w^2 + 0.2952C_{101}^2 \\ & + 0.0860T_w \cdot C_{101} - 0.0775T_w \cdot C_{Z01} - 0.1909C_{101} \cdot C_{Z01} \end{aligned} \quad (52)$$

Likewise, \hat{t}_{cycle}^1 uses the same scaling scheme as \hat{t}_{z1} and with a R^2 value of 99%. This response is described by the regression meta-model:

$$\begin{aligned} \hat{t}_{\text{cycle}}^1 = & -0.6243 - 0.2634T_w - 0.4244C_{101} + 0.2171C_{Z01} + 0.0622T_w^2 + 0.2158C_{101}^2 \\ & + 0.0022C_{101}^2 + 0.1407T_w \cdot C_{101} - 0.0533T_w \cdot C_{Z01} - 0.1269C_{101} \cdot C_{Z01} \end{aligned} \quad (53)$$

The only response that did not need a meta-model was t_{f1} because of the simplicity of the model used. Once many of the parameters of the model for t_{f1} have been specified, this reduces to the following expression:

$$t_{f1} = 1.0664 \times 10^{-5} (14.287 e^{800/T_w})^{1/0.315} \quad (54)$$

where T_w must be expressed in kelvins.

The decision to involve either physics based models or empirical models has a lot to do with the objective of each specific analysis. This case was developed with optimization in mind following the decision process described in figure 1.

6. Production of an injection moulded part

For completeness of the discussion of empirical modelling, we will present an example relating to thermoplastic IM. This case will lead the way to present the use of DEA later in this document. Consider the part of constant thickness $h = 3$ mm shown in figure 17. The part is intended to be injection moulded in a Sumitomo IM machine using polyethylene terephthalate (PET; Ticona IMPET EKX-210). Three PMs were included in this study: (1) maximum injection pressure,

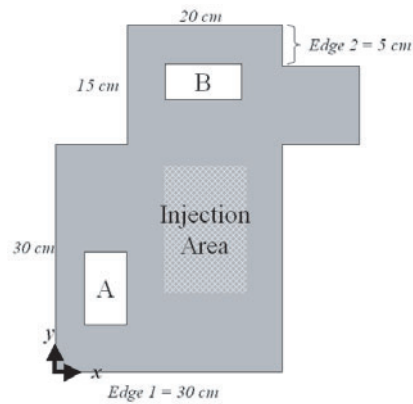


Figure 17. Part of constant thickness with cut-outs.

Table 3. Summary of performance and results from residual analysis results for the regression meta-models.

	P_1	t_f	R_z
<i>Performance</i>			
R^2 (%)	96.6	99.45	96.17
MAPE (%)	3.63	1.71	27.96
MAPE validation (%)	8.632	2.031	15.29
<i>Residual</i>			
Normality	Yes	Yes	Yes
Independence	Yes	Yes	Yes
Constant variance	Yes	Yes	Yes

P_1 , (2) time to freeze, t_f , and (3) range of part deflection in the z -direction, R_z . For production purposes, it is desirable to minimize all of the PMs identified above with the following aims: P_1 to keep the machine capacity unchallenged; t_f to reduce our total cycle time; and R_z to provide dimensional control.

Each of these PMs can be estimated using CAE software, specifically Moldflow™ [25]. Under the characteristics of the machine specified above and at specific combinations of the following controllable variables: (i) melt temperature, T_m , (ii) mould temperature, T_w , (iii) ejection temperature, T_e , (iv) horizontal coordinate of the injection point, x and (v) vertical coordinate of the injection point, y . These last two variables are related to the decision of where to locate the injection point considering only the injection area shown on figure 17. The injection area is constrained due to physical limitations of the IM machine.

A finite element mesh of the part was created in order to obtain the estimates of the PMs via Moldflow™. The first data set was then created by conducting a full factorial experimental design of the five controllable variables at discrete levels within an experimental region recommended by the software's material database [2]. The creation of three meta-models (one per PM) with the use of the first data set followed.

The results of the fitting performance of the regression meta-models obtained for each of the three PMs are presented on table 3. Also reported in table 3 is the MAPE for a validation data set (a set of points obtained experimentally not used to fit the meta-model). This second MAPE is useful to understand the prediction capabilities of the meta-model.

Because DEA relies heavily on the prediction of PMs at a large amount of untried combinations of controllable variables, it was worthwhile to try to fit meta-models that allowed

Table 4. Summary of performance for the ANNs.

	P_1	t_f	R_z
<i>Performance</i>			
R^2 (%)	99.98	99.99	99.1
MAPE (%)	0.2	0.21	8.6
MAPE validation (%)	3.66	0.24	6.68

obtaining closer predictions within the experimental region of interest. With this in mind, the performance of the ANNs obtained is presented table 4.

It is worth mentioning that when fitting the ANNs, it was an explicit goal to achieve better prediction capability than that obtained through linear regression. This was achieved by allowing the training of the neural networks stop at the point where the prediction error started to deteriorate. The results are evident when comparing the MAPE values for the validation set in tables 3 and 4.

7. Applications of simulation and optimization

Thus far, a series of case studies with different kinds of model characteristics have been reviewed. However, although modelling might be a goal by itself, in the majority of cases the models are used to simulate and select suitable process alternatives (see figure 1). Finding these alternatives is most effectively done through formal optimization techniques.

As discussed previously, in actual industrial processes having more than one PM that needs to be addressed simultaneously is the rule rather than the exception. Furthermore, improving a PM can frequently be done only by detriment of other PMs, therefore imposing a compromise. Finding settings of controllable variables to optimize several PMs is a task commonly known as a multiple criteria optimization problem. DEA has been used to solve this type of problems in polymer processing in previous studies [1–3].

DEA, a technique developed by Charnes *et al* [44], provides a way to measure the efficiency of a given combination of PMs relative to a finite set of combinations of PMs of similar nature. The efficiency of each combination is computed through the use of two linearized versions of the following mathematical programming problem in ratio form:

$$\begin{aligned} &\text{Find} \quad \nu, \mu, \mu_0 \text{ to} \\ &\text{Maximize} \quad \frac{\mu^T Y_0^{\max} + \mu_0}{\nu^T Y_0^{\min}} \end{aligned} \quad (55)$$

s.t.

$$\frac{\mu^T Y_j^{\max} + \mu_0}{\nu^T Y_j^{\min}} \leq 1 \quad j = 1, \dots, n \quad (56)$$

$$\frac{\mu^T}{\nu^T Y_0^{\min}} \geq \varepsilon \cdot 1 \quad (57)$$

$$\frac{\nu^T}{\nu^T Y_0^{\min}} \geq \varepsilon \cdot 1 \quad (58)$$

$$\mu_0 \text{ free} \quad (59)$$

where, Y_0^{\max} and Y_0^{\min} are vectors containing the values of the PMs of the combination currently under analysis to be maximized and minimized, respectively, Y_j^{\max} and Y_j^{\min} are vectors containing the values of the PMs of the j th combination to be maximized and minimized,

respectively, μ is a vector of multipliers for all the PMs to be maximized, ν is a vector of multipliers for all the PMs to be minimized, μ_0 is a scalar variable, n is the number of total combinations in the set, and ε is a very small constant usually set to a value of 1×10^{-6} .

The efficiency score obtained from solving the problem formulated above for each combination ranges from 0 to 1 and is relative to all n combinations. Those combinations with efficiency of 1 are deemed efficient. The collection of the efficient combinations makes up the (piece-wise) efficient frontier of the entire set. These efficient combinations dominate any other combination not in the frontier.

Linearization of the problem described by equations (55)–(59) becomes necessary because the ratio format of the original formulation results in an infinite number of solutions [45]. Linearization is achieved by setting the denominator of equation (55) to a value of 1, while multiplying both sides of equation (56) by the denominator of its left-hand side; the inequalities in equations (57) and (58) are simplified once the denominator takes the value of 1; and equation (59), can be decomposed into the difference of two non-negative variables [3]. Following these manipulations, one obtains the first linear version of the problem, called the input oriented model [45].

The second linearization is obtained by inverting the ratios in the original formulation (equations (55)–(59)) and keeping the variable μ_0 in the numerator in equations (55) and (56). The rest of the linearization steps are similar to those described earlier. The original formulation will then be transformed into a minimization problem, with equation (56) being a lower bound constraint. The efficiency in this second problem, called the output oriented model, ranges from 1 to ∞ with 1 being the perfect efficiency score. A particular combination will be considered efficient when both the input oriented and the output oriented models identify it as efficient.

DEA is a non-parametric approach (i.e. a data-driven approach), as implied by its name. This characteristic eliminates the need for the analyst to decide upon specific ‘weights’ for the different PMs, thereby keeping the objectivity of the analysis. The linearized DEA versions described previously can be effectively solved with the simplex method, which is included in practically every major commercially available optimization software package. The only potential burden in the application of DEA might come from repeating the task n times (once for each of the n combinations). However, it is our believe that by properly computer-coding this routine the analysis can be achieved in a reasonable amount of time.

The analytic functions obtained through empirical modelling in the IM case described previously for the part shown in figure 17 can be used to produce large amounts of predictions for the PMs in short time. This capability along with their simplicity makes them ideal for optimization, and in this case, for DEA. In order to carry out a DEA, one must create a second data set containing as many PMs predictions as practicality dictates in the experimental region of interest. Because sampling of the experimental region is the analyst’s decision, the choice was to do it by generating a factorial enumeration with T_m and T_w at five levels, and the rest of the variables (T_e , x , and y) at three levels. The factorial process produced 675 combinations of controllable variables at which predictions of each of the three PMs were made.

Because all three PMs were to be minimized, at least one of them had to be transformed to provide the maximization instance required for equations (55) and (56). The transformation is achieved with the use of the following expression:

$$\psi_j^* = (\psi_{\max} + \psi_{\min}) - \psi_j \quad j = 1, \dots, n \quad (60)$$

where ψ_{\max} and ψ_{\min} are the maximum and minimum values of the untransformed PM and ψ_{\max} is the j th value of the untransformed PM.

The results of the DEA, obtained by following the process described in the DEA section, are graphically shown in figure 18. Notice that out of the 675 combinations of predicted

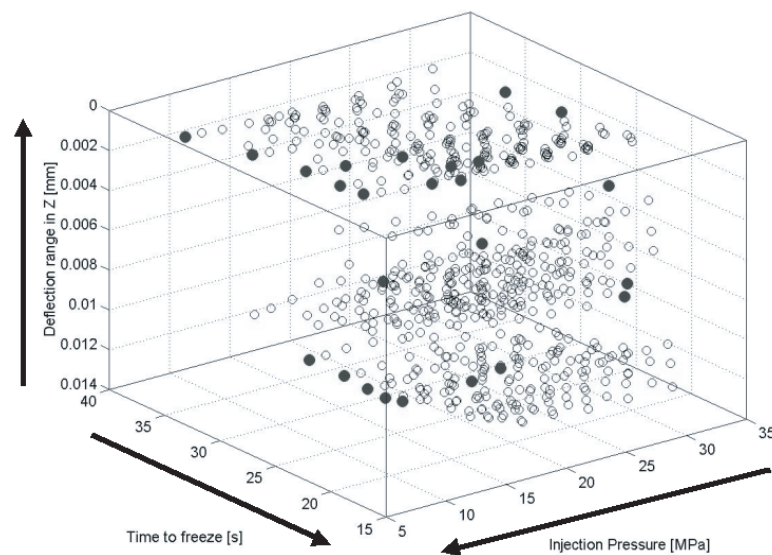


Figure 18. DEA results: the solid spheres represent the efficient combinations (best compromises), the hollow spheres are the dominated combinations, and the arrows indicate the desired optimization direction.

PMs, DEA identified the 25 that were efficient, that is the best compromises between the three PMs. These best compromises can then be traced back to the combinations of controllable process and design variables that originated them. All this information is readily available in the factorial design used to sample the experimental region.

In order to further support the use of a multiple criteria optimization technique such as DEA, let us consider the optimization case with a single PM. If P_1 is chosen as the sole PM to be minimized in the experimental area of interest, the optimal point is found at $(T_w, T_m, T_e, x, y) = (140^\circ\text{C}, 290^\circ\text{C}, 149^\circ\text{C}, 150\text{ mm}, 250\text{ mm})$, which yields a predicted P_1 value of 9.33 MPa. A confirmation run in Moldflow verifies that this solution is as good as the best run obtained in the first experimental data set. However, this optimal point, when used to predict t_f and R_z , gives a value of 37.8 s and 0.001 mm, respectively. The value for t_f is very high. Although, one might consider including t_f and R_z as part of the optimization so that these PMs would not go above a certain threshold, the definition of this threshold will introduce a bias in the result, since it would depend on the interests of the analyst. Furthermore, if a different PM is chosen as the objective function, the results might be completely different. For example, in the case where t_f is chosen as the objective function, the optimal point obtained is $(T_w, T_m, T_e, x, y) = (120^\circ\text{C}, 260^\circ\text{C}, 159^\circ\text{C}, 150\text{ mm}, 250\text{ mm})$ with a predicted value for t_f of 17.16 s (also verified to be a good solution with a confirmation run). This optimal point for t_f results in a value for P_1 of 16.61 MPa, and of 0.008 mm for R_z . In this case, both of the other PMs are undesirably high.

The advantage of considering all three PMs as shown here is that one can easily visualize the compromises between all of them, and choose a combination deemed convenient explicitly knowing the impact of our choice. The visualization for this case study is shown in figure 19. Referring to this figure, one can see that when the best compromises are ordered in terms of increasing injection pressure, there seems to be a correlation between this PM and the time to freeze, while the deflection range in the z -direction does not seem to correlate with any of the other PMs. Also note that options with values similar to those described in the single

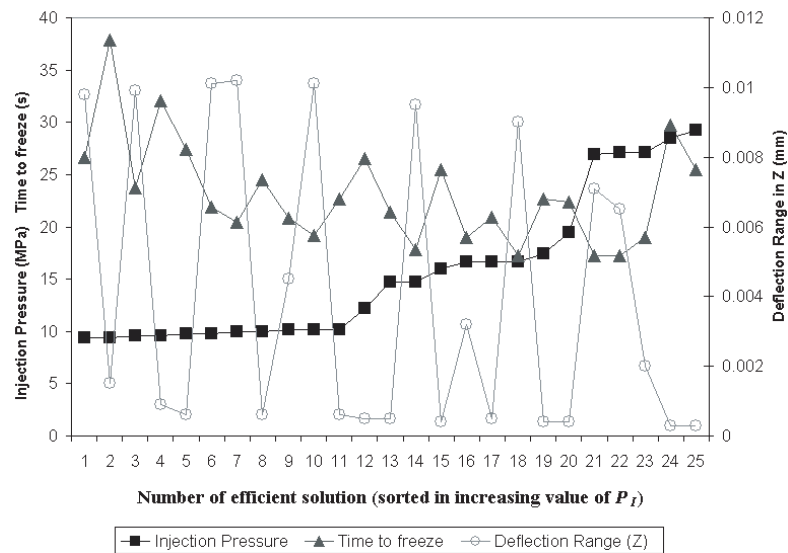


Figure 19. Visualization of compromises in the efficient solutions.

criteria optimization were also identified in this analysis, with the additional information on the trade-offs implied by each choice. This result is important because the efficient solutions were identified by a data-driven approach (non-parametric), resulting in unbiased conclusions.

Another important consideration has to do with the fact that, although it might look appealing to find efficient solutions graphically in two- and three-dimensional cases, this might not be convenient effort-wise. Furthermore, higher dimensionality precludes the use of graphical methods, making techniques such as DEA an even more attractive option. Consider, for example, the case of production of in-mould coated SMC parts described earlier. Using the same data generation process based on simulation of untried combinations generated through full factorial designs, the multiple criteria optimization problem was then solved by identifying the best compromises through DEA between the four following PMs: (1) total cycle time (SMC compression moulding + IMC); (2) Ashland Index; (3) rate of change of the final part dimensional variation w.r.t. moulding temperature; and (4) rate of change of the final part dimensional variation w.r.t. filler content. The results are shown in figure 20. The efficient solutions presented in figure 20 are sorted in increasing value of total cycle time. This order allows observing what seems to be a strong negative correlation between cycle time and the Ashland Index. The same is true between both rates of change. These observations should lead to further the exploration of the relationships between these performance measurements as well as their physical causes. As mentioned previously, the efficient solutions can be traced back to the settings of the controllable variables that produced them since they are retained in the factorial enumeration. Further analysis of the resulting settings may reveal regions with the potential to provide the process with robustness.

8. Conclusions

In this paper, the areas of modelling and simulation in reactive polymer processing were reviewed with an emphasis on model building. For completeness we included one example on thermoplastic IM. The use of both types of models, physics based and empirical ones, were

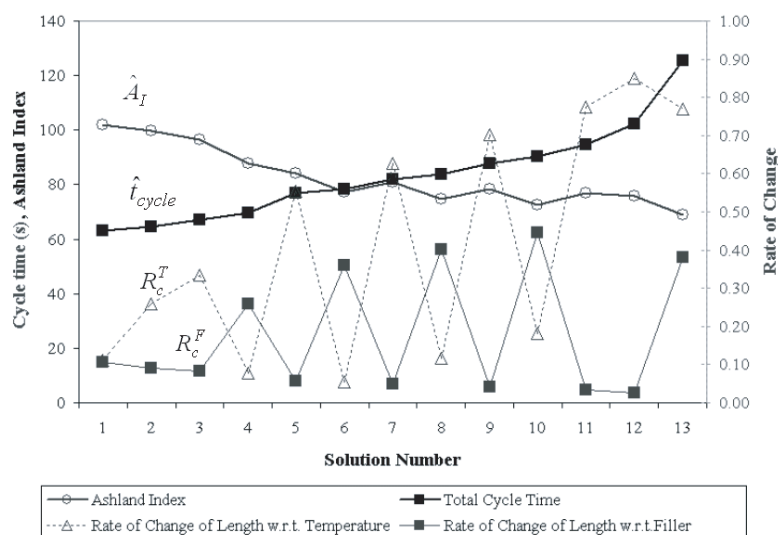


Figure 20. Values of \hat{A}_I , \hat{t}_{cycle} , R_c^T , and R_c^F identified as the best compromises and plotted vs the efficient solution number ordered in increasing value of \hat{t}_{cycle} .

described through several case studies and a general decision-making framework to process modelling was introduced. Special consideration was given to demonstrate how techniques such as scaling analysis and experimental design can simplify both the modelling and simulation efforts. Additionally, the importance of considering several PMs simultaneously through formal optimization techniques was underlined. DEA was also reviewed as a viable approach to multiple criteria optimization and consequently to find the best process alternatives in terms of controllable variables. Modelling itself allows for a compromise between different aspects: available knowledge on the phenomena of interest, complexity of the competing models, and ultimately, availability of resources to use these models (simulate) to generate predictions. This review intended to structure these aspects and point to helpful support techniques to ultimately arrive at attractive process alternatives in polymer processing.

References

- [1] Cabrera-Ríos M, Castro J M and Mount-Campbell C A 2004 Multiple quality criteria optimization in reactive in-mold coating with a data envelopment analysis approach II: a case with more than three performance measures *J. Polym. Eng.* accepted
- [2] Castro C E, Cabrera-Ríos M, Lilly B, Castro J M and Mount-Campbell C A 2003 Identifying the best compromises between multiple performance measures in injection molding (IM) using data envelopment analysis (DEA) *J. Integrated Des. Process Sci.* **7**:1 77–87
- [3] Cabrera-Ríos M, Castro J M and Mount-Campbell C A 2002 Multiple quality criteria optimization in in-mold coating (IMC) with a data envelopment analysis approach *J. Polym. Eng.* **22** 5
- [4] Dantzig J A and Tucker III C L 2001 *Modeling in Materials Processing* (Cambridge: Cambridge University Press)
- [5] Castro J M and Lee C C 1989 *Model Simplification, Fundamentals of Computer Modeling for Polymer Processing* ed E C Bernhardt and C L Tucker (Munich: Hanser)
- [6] Castro J M and Macosko C W 1982 Studies of mold filling and curing in the reaction injection molding process *AIChE J.* **28** 250
- [7] Macosko C W 1989 *Fundamentals of Reaction Injection Molding* (New York: Hanser)
- [8] Kolodziej P, Macosko C W and Ranz W E 1982 The influence of impingement mixing on striation thickness distribution and properties in fast polyurethane polymerization *Polym. Eng. Sci.* **388** 9

- [9] Chella R and Ottino J M 1983 Modeling of rapidly-mixed, fast-crosslinking, exothermic polymerizations *AIChE J.* **29** 373
- [10] Estevez S and Castro J M 1984 Applications of a RIM process model in the analysis of premature gelling, demold time and maximum temperature rise *Polym. Eng. Sci.* **24** 428
- [11] Domine J D and Gogos C G 1980 Simulation of reactive injection molding *Polym. Eng. Sci.* **20** 843
- [12] Coyle D J, Blake J W and Macosko C W 1987 The kinematics of fountain flow in mold filling *AIChE J.* **33** 1168
- [13] Castro J M 1980 *PhD Thesis* University of Minnesota
- [14] Manzione L T 1981 Simulation of cavity filling and curing in reaction injection molding *Polym. Eng. Sci.* **21** 1234
- [15] Manas-Zloczower I and Macosko C W 1986 Moldability diagrams for reaction injection molding *Polym. Process Eng.* **4** 173
- [16] Manas-Zloczower I and Macosko C W 1981 Moldability diagrams for reaction injection molding of a polyurethane crosslinking system *Polym. Eng. Sci.* **19** 1229
- [17] Manas-Zloczower I, Blake J W and Macosko C W 1987 Space-time distribution in filling a mold *Polym. Eng. Sci.* **27** 1229
- [18] Castro J M and Griffith R M 1993 *Sheet Molding Compounds Science and Technology* ed H G Kia (New York: Hanser) p 163
- [19] Castro J M, Melby E G and Griffith R M 1988 SMC technology: past, present, future *Autom. Polym. Des.* **8** 28–34
- [20] Melby E and Castro J M 1989 *Comprehensive Polymer Science* ed S G Allen (New York: Pergamon)
- [21] Castro J M and Griffith R M 1997 *Composites Engineering Handbook* ed P K Mallick (New York: Marcel Dekker)
- [22] Straus J E, McBain D and Wilczek F 1997 Advances in in-mold coating *Reinforced Plast.* **41** 34–40
- [23] Castro J M 1996 *Innovation in Polymer Processing Molding* ed J F Stevenson (New York: Hanser)
- [24] Cabrera-Ríos M, Zuyev K S, Chen X, Castro J M and Straus E J 2002 Optimizing injection gate location and cycle time for the in-mold coating (IMC) process *Polym. Compos.* **23** 723–738
- [25] www.moldflow.com
- [26] Box G E P, Hunter W G and Hunter J S 1978 *Statistics for Experimenters: An Introduction to Design, Data Analysis, and Model Building* (New York: Wiley)
- [27] Montgomery D C 1997 *Design and Analysis of Experiments* (New York: Wiley)
- [28] Box G E P and Draper N R 1987 *Empirical Model Building and Response Surfaces* (New York: Wiley)
- [29] Seber G A F 1977 *Linear Regression Analysis* (New York: Wiley)
- [30] Fausset L 1994 *Fundamentals of Neural Networks: Architectures, Algorithms, and Applications* (Upper Saddle River: Prentice Hall)
- [31] Sarle W S 1994 Neural networks and statistical models *Proc. 19th Annual SAS Users Group Int. Conf.*
- [32] Funahashi K 1989 On the approximate realization of continuous mappings by neural networks *Neural Netw.* **2** 183
- [33] Hornik K 1991 Approximation capabilities of multilayer feedforward networks *Neural Netw.* **4** 251
- [34] Hagan M T, Demuth H B and Beale M 1996 *Neural Network Design* (Boston: PWS)
- [35] Chambers M and Mount-Campbell C A 2002 Process optimization via neural network metamodeling *Int. J. Prod. Econ.* **79**
- [36] Hupp S S 1998 A quantitative method for analysis of surfaces of molded SMC parts *43rd Annu. Conf. Proc.: The Society of Plastics Industry* session 10-A
- [37] Castro J M and Melby E G 1989 *Glass-Reinforced Thermosetting Polyester Molding: Materials and Processing* ed S L Aggarwal (Akron: Pergamon)
- [38] Stevenson J F 1986 Free radical polymerization models for simulating reactive processing *Polym. Eng. Sci.* **26** 46
- [39] Lee L J 1981 Curing of compression molded sheet molding compound *Polym. Eng. Sci.* **21** 483–492
- [40] Castro J M and Lee C C 1987 Thermal and cure analysis in sheet molding compound compressing molds *Polym. Eng. Sci.* **27**
- [41] Zuyev K S and Castro J M 2002 Applications of chemo-rheology to develop process windows in reactive in-mold coating *J. Polym. Eng.* **22** 233–259
- [42] Abrams L and Castro J M 2003 Predicting molding forces during sheet molding compound (SMC) compression molding I: model development *Polym. Compos.*
- [43] Boyan S, Abrams L and Castro J M 2003 Predicting molding forces during sheet molding compound (SMC) compression molding II: effect of SMC composition *Polym. Compos.* **24** 731–747
- [44] Charnes A, Cooper W W and Rhodes E 1978 Measuring the efficiency of decision making units *Eur. J. Oper. Res.* **2** 429–444
- [45] Charnes A, Cooper W W, Lewin A Y and Seiford L M 1993 *Data Envelopment Analysis: Theory, Methodology, and Applications* (Boston: Kluwer)